Ceramics International 49 (2023) 30536–30546

Contents lists available at ScienceDirect

Ceramics International

journal homepage: www.elsevier.com/locate/ceramint

Unravelling the role of the exchanged Ni amount in zeolites A and X for their thermal transformation into magnetic metal-ceramic nanocomposites

Olimpia Tammaro [a], Gabriele Barrera [b], Paolo Allia [a,b], Paola Tiberto [b], Antonello Marocco [c], Maela Manzoli [d], Barbara Bonelli [a], Giorgia Confalonieri [e], Rossella Arletti [f], Michele Pansini [c], Serena Esposito [a,*]

[a] Department of Applied Science and Technology and INSTM Unit of Torino – Politecnico, Politecnico di Torino, Corso Duca degli Abruzzi 24, 10129, Torino, Italy
[b] INRiM Torino, Advanced Materials for Metrology and Life Sciences, Strada delle Cacce 91, 10143 Torino, Italy
[c] Department of Civil and Mechanical Engineering and INSTM Research Unit, Università degli Studi di Cassino e del Lazio Meridionale, Via G. Di Biasio 43, Cassino, FR 03043, Italy
[d] Department of Drug Science and Technology, NIS Interdepartmental Centre and INSTM Unit of Torino - University of Torino, Via Giuria 9, Torino, 10125, Italy
[e] ID22 beamline, European Synchrotron Radiation Facility (ESRF), 71 Av. des Martyrs, Grenoble, 38000, France
[f] Università degli Studi di Modena e Reggio Emilia, Chemical and Geological Sciences, Via Campi 103, Modena, 41125, Italy

ARTICLE INFO

Handling Editor: Dr P. Vincenzini

Keywords:
Magnetic zeolites
Nanocomposites
Magnetic Ni-Nanoparticles

ABSTRACT

Magnetic zeolites with a Ni content of 4.80 and 6.20 wt%, were prepared by Ni-exchanging zeolites 4 A and 13×, respectively, and thermally treating the Ni-exchanged zeolites at 735–750 °C, under a reducing atmosphere. This thermal treatment gave rise to the formation of Ni^0 nanoparticles dispersed in a ceramic matrix, which partially retained the zeolitic structure (about 50%). The obtained nanocomposites were fully characterized using atomic absorption spectrometry, X-rays powder diffraction (with synchrotron source) followed by Rietveld analysis, High-Resolution Transmission Electron Microscopy, N_2 adsorption/desorption at −196 °C and magnetic measurements at both room temperature and low temperature. To highlight the effect of nickel content on the final properties of the nanocomposites, the features of the samples produced in this work were compared with the features of the nanocomposites obtained, in previous works, from the same zeolites loaded with a low (approx. 1%) and a high (approx. 15 wt%) Ni content.

The most important result obtained here is that only by entering the intermediate Ni content of this work (4.80–6.20 wt%) it was possible to obtain real magnetic zeolites as the final product of the process. The low Ni content gave rise to a poor magnetic response, whereas the high Ni content resulted in the almost total destruction of the zeolite framework.

1. Introduction

In the last few decades, the widespread interest towards nanomaterials and nanocomposites has triggered several experimental techniques and innovative processes aiming at their production with higher efficiency and at lower cost [1]. Such interest stems from the fact that particles, with dimensions below a critical value, exhibit properties that in their bulk homologous are missing [2–9]. Moreover, more and more appealing materials could be obtained, if the manufactured nanomaterials and nanocomposites exhibited a magnetic behaviour, together with the properties deriving from their nanometric dimensions [10–15].

Among such innovative processes, the one proposed by some of us a few years ago exhibits potential for practical application owing to its low cost, high efficiency, large simplicity and high versatility. This process consists of thermally treating at relatively moderate temperatures (500–850 °C) commercial zeolites exchanged with transition metal cations under a reducing atmosphere. The product of these operations is a composite formed by the transition metal nanoparticles (with a size of a few or tens nanometers) evenly dispersed in a prevailingly amorphous silica and alumina matrix, which keeps at least a part of the original porosity, typical of the zeolite precursor [16–18]. These nanocomposites were successfully used in biochemical and environmental applications and as valid moon dust simulants [19–23]. All the metal-ceramic nanocomposites produced through the described process exhibit

* Corresponding author.
E-mail address: serena_esposito@polito.it (S. Esposito).

https://doi.org/10.1016/j.ceramint.2023.07.003
Received 28 March 2023; Received in revised form 28 June 2023; Accepted 2 July 2023
Available online 8 July 2023

magnetic properties owing to the presence of nanoparticles of ferromagnetic metals such as Fe^0, Co^0 and Ni^0 dispersed in the ceramic matrix prevailingly formed by a silica-alumina amorphous phase. Moreover, it must be said that such magnetic metal nanoparticles are small (5–25 nm) and stable towards oxidation as they are protected by the ceramic matrix wherein they are embedded.

Recently, a slight and simple modification of this technique allowed obtaining the dispersion of magnetic metal nanoparticles (5–30 nm) within original microporous zeolite structures, thus obtaining real magnetic zeolites. Consequently, very interesting technological properties are expected from these materials.

Among the advantages presented by the technique of thermal transformation of heavy metal cation exchanged zeolites, under a reducing atmosphere, in magnetic metal-ceramic nanocomposites and magnetic zeolites, the versatility must be evidenced. Actually, whoever produces such materials has at his disposal a number of different key parameters to properly tune their technological properties. In particular, a wise choice of the parent zeolite, heavy metal cation(s), cation exchange procedures, temperature and time of the thermal treatment under reducing atmosphere, nature of the reducing agent, type of reactor where the thermal treatment is performed, were found to, possibly, result in substantial, positive changes of the technological features of the final products of the process [24].

A systematic investigation of the extent to which the variation of the previously reported key parameters affects the technological properties of the final products was not undertaken yet and, indeed, appears an overwhelming task given the complexity of the cross effects that should be recorded. Thus, this last one appears a still largely unexplored research field, as only very partial insights into the potential for practical applications of these techniques were attained. However, some step ahead in this direction was already performed. In particular, the study and the interpretation of the magnetic behaviour of these nanocomposites, which represented a great challenge even from the fundamental point of view, triggered three other works about this subject. The first and the second concerned the magnetic behaviour of the nanocomposites obtained from the thermal treatment under reducing atmosphere of Ni-exchanged zeolites A and X bearing about the highest possible Ni content [24,25]. The third regarded the magnetic behaviour of the nanocomposites obtained from the thermal treatment under reducing atmosphere of weakly Ni-loaded zeolites A and X [26]. In these works, only the amount of Ni^{2+} exchanged by A and X zeolites changed, whereas all the other key parameters were kept constant. The magnetic metal-ceramic nanocomposites, produced within these works, were fully characterized from the chemical, compositional, mineralogical, textural, and magnetic points of view.

Based on the previous considerations, the preparation of magnetic metal-ceramic nanocomposites obtained from the thermal treatments under reducing atmosphere of Ni-exchanged zeolites A and X bearing a Ni content intermediate between those of the works [24–26] *(ceteris paribus)*, and their similar characterization [17,23,25], appears to, possibly, supply further insight in the extent to which the variation of the heavy metal cation exchange procedures (in practice the variation of the amount of exchanged heavy metal cation) affects the features of the magnetic metal-ceramic nanocomposites final products of this process. This is the first goal of this work.

Moreover, this work intends to demonstrate how a wise choice of one of the key parameters affecting the described technique of thermal treatment of heavy metals exchanged zeolites under a reducing atmosphere (in this case the modalities of the cation exchange operations) may be crucial in obtaining materials that, although keeping all the properties of zeolites (i.e. microporosity, cation exchange, adsorption, catalytic behaviour), exhibit also a magnetic behaviour. In a few words, this work intends to demonstrate how a proper choice of cation exchange modalities may result in obtaining real magnetic zeolites.

2. Experimental

2.1. Synthesis of the nanocomposites

Carlo Erba reagent grade 4 A zeolite (framework type LTA [27], $Na_{12}Al_{12}Si_{12}O_{48}27H_2O$, hereafter referred to as "Na-A zeolite") and 13× zeolite (framework type FAU [27], $Na_{86}Al_{86}Si_{106}O_{384}264H_2O$, hereafter referred to as "Na-X zeolite") were used. Their cation exchange capacity (as determined by the "batch exchange method" [28,29]) was very close to the calculated cation exchange capacity of 5.48 and 4.73 meq g^{-1} for A and X zeolite, respectively.

The exchange solution was prepared by dissolving Carlo Erba reagent grade 99.5 wt% $NiCl_2{\cdot}6H_2O$, nickel (II) chloride hexahydrate, in doubly distilled water. Doubly distilled water was used to avoid interference of external cations in ion exchange. The parent A and X zeolites were contacted with a $[Ni^{2+}] = 0.01$ M solution with a solid/liquid weight ratio of 1/100 and contact time (t) = 2 h at about 70 °C. The solid was separated from the liquid by filtration and abundantly washed with doubly distilled water: particular care was devoted to this last operation to completely remove Cl^-, as confirmed by EDS analyses carried out on Ni nanocomposite materials. Indeed, the presence of chlorine can be detrimental to some technological applications. Then, the Ni-exchanged zeolites were dried for about one day at 80 °C, and stored for at least 3 days in an environment with about 50% relative humidity to allow water saturation of the zeolite.

Two aliquots of each Ni^{2+} exchanged zeolite (both NiA and NiX) were subjected to two different thermal treatments under a reducing atmosphere (*i.e.* a flow of a gaseous mixture containing 2 vol % H_2 in Ar) in an alumina tubular furnace (inner diameter = 6.9 cm, lenght = 91 cm), using Pt crucibles. Thus, four different samples of metal-ceramic nanocomposite materials (labelled as follows) were obtained.

1) The NiA735C-12min and NiX735C-12min samples were obtained by heating from room temperature (r.t.) to 735 °C (15 °C min^{-1} heating rate) and a subsequent isothermal step at 735 °C for 12 min. The heating system of the furnace was then switched off and the sample was left to cool down to r.t. within the furnace.
2) The NiA750C-0min and NiX750C-0min samples were obtained by heating from r.t. up to 750 °C (15 °C min^{-1} heating rate) and then by switching off the heating system as soon as the temperature of 750 °C was reached. The samples were left to cool down to r.t. within the furnace.

Both the temperature and times of thermal treatments were chosen to investigate their role in the production of magnetic nanocomposites and to keep uniformity with previous works [26,30].

2.2. Methods

The Ni^{2+} and (residual) Na^+ contents of NiA and NiX zeolites were determined by dissolving the zeolite in a 40 wt% HF and 14 wt% $HClO_4$ aqueous solution and by determining the Ni^{2+} and Na^+ contents using atomic absorption spectrophotometry (AAS, PerkinElmer Analyst 100 apparatus) [31,32].

Textural properties were determined based on the nitrogen and carbon dioxide adsorption isotherms at −196 °C and 0 °C, respectively (Micrometrics ASAP 2020). Before the measurement, the sample was outgassed under a high vacuum at 200 °C for 3 h to remove pollutants previously adsorbed. From the nitrogen adsorption isotherms, the specific surface area (SSA) of the samples was calculated according to the BET (Brunauer–Emmet–Teller) method or the Langmuir equation. Micropore volume, V_{mp}, was calculated by applying the *t*-plot method and the total pore volume, Vp, was determined from the amount of adsorbed N_2 at $P/P^0 = 0.98$. For carbon dioxide isotherm, the specific surface area and total pore volume have been calculated by applying the Dubinin-Radushkevich method.

Quantitative phase analyses (QPA) of the nanocomposites were performed by using synchrotron radiation XRPD (experiments performed on the high-resolution beamline ID22 at ESRF (Grenoble), using the new Extremely Brilliant Source and a fixed wavelength of 0.354196 Å). Samples were packed in a borosilicate glass capillary and spun under the beam; the diffraction patterns were collected using an Eiger2 X CdTe 2M – W detector preceded by nine Si (111) analyser crystals. The combined RIR-Rietveld method was used to allow the quantification of both the crystalline and amorphous fractions. Thus, 10 wt % of Al_2O_3 was added to each sample as internal standard, to allow the re-calculation of the real amount of crystalline phases [33]. All the refinements were performed by using the Topas software in launch mode with Jedit [34]. The structures of NiA and NiX [17] were used as initial models, only the occupancy factors of the extra framework species were refined to account for the effect of the thermal treatment.

The samples were characterized by High-Resolution Transmission Electron Microscopy (HRTEM) by using a 300 kV JEOL 3010-UHR instrument equipped with a LaB_6 filament. Digital micrographs were acquired by a (2 k x 2 k)-pixel Ultrascan 1000 CCD camera and were processed by Gatan digital micrograph. Before the analyses, each sample in the form of powder was contacted with a lacey carbon Cu grid, which resulted in the adhesion of some particles to the sample holder by electrostatic interactions. Such a procedure guaranteed to obtain a good dispersion of the sample particles and avoided any modification induced by the use of a solvent. Histograms of the Ni particle size distribution were obtained by considering a representative number of particles for each sample (>200 for NiA735-12nim and NiX735-0min, >500 in the case of NiA750-0min and NiX750-0min) and the mean particle diameter (d_m) was calculated as:

$$d_m = \Sigma d_i n_i / \Sigma n_i$$

where n_i is the number of particles of diameter d_i.

Ni particles appear well contrasted with respect to the zeolite matrix and the counting was performed on electron micrographs obtained starting from 20,000 × magnification.

The magnetic properties of the nanocomposites were studied at both r.t. and low T (5 K) by using a SQUID magnetometer operating in the 0–70 kOe range. The FC/ZFC curves of Ni-rich zeolites were obtained under a field of 200 Oe in the temperature interval 10–300 K using the Lakeshore VSM.

3. Results and discussion

3.1. Chemical composition and quantitative phase analysis of NiA and NiX zeolites

According to AAS chemical analysis, the NiA sample contains 164 meq/100 g Ni^{2+} and 375 meq/100 g Na^+, and the NiX sample contains 211 meq/100 g Ni^{2+} and 254 meq/100 g Na^+. The corresponding cation equivalent fractions of $x_{Ni} = 0.31$ and $x_{Na} = 0.69$ (NiA sample), and $x_{Ni} = 0.45$ and $x_{Na} = 0.55$ (NiX sample) were calculated.

The weight percentage of Ni (wt. % Ni) in the final nanocomposites, NCs, calculated based on the Ni^{2+} content of the exchanged zeolites by considering the final NCs as completely dehydrated materials, was 4.80 and 6.20 wt% Ni in the NCs derived from NiA and NiX, respectively.

The observed and calculated patterns deriving from Rietveld refinement are reported in Fig. 1a, b, 1c and 1d, while the results of the quantitative phase analysis (QPA) along with the data obtained for zeolite Ni-A and Ni-X bearing a low Ni (ref. [18,26]) and a high Ni content (ref. [24,25]), which underwent homologous thermal treatment under reducing atmosphere, are reported in Table 1. Although the series analysed here (NiX and NiA) behave similarly, nickel-exchanged zeolite

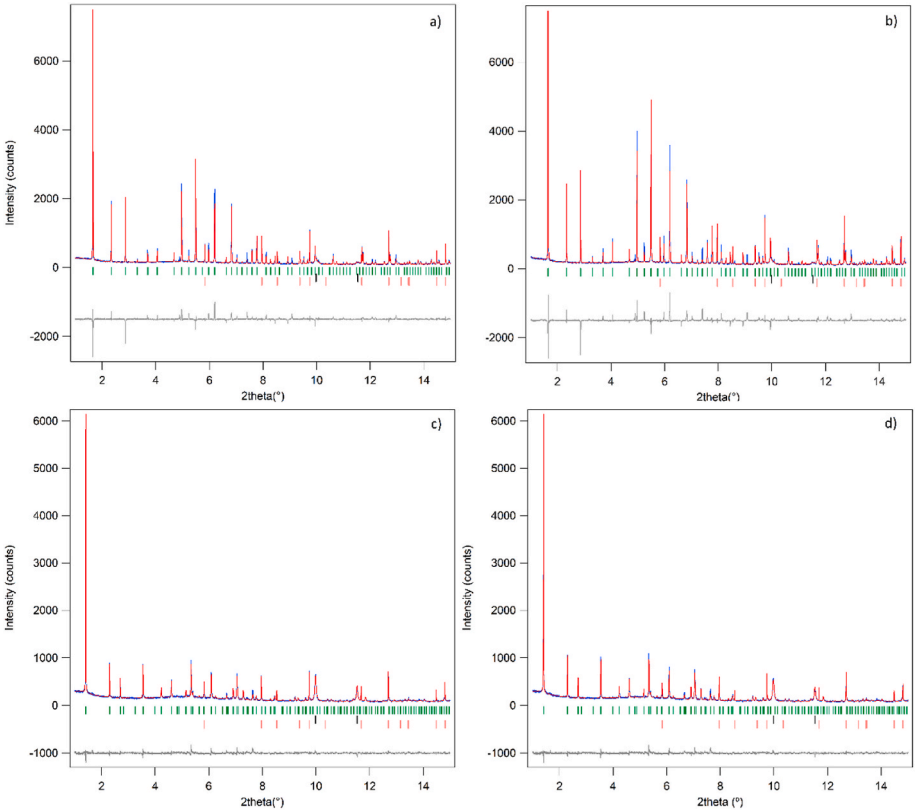

Fig. 1. Observed (blue lines) and calculated (red lines) diffraction patterns and final difference curve (grey line) from Rietveld refinements of samples NiA735C-12min (a), NiA750C-0min (b), NiX 735C-12min (c) and NiX 750C-0min (d). Tick marks refer to the different phases: green for NiA (a and b) and NiX (c and d), orange for a-Al2O3 standard and black for nickel. (For interpretation of the references to colour in this figure legend, the reader is referred to the Web version of this article.).

Table 1
Results of quantitative phase analyses (QPA) and magnetic data. Errors are not reported, indeed, due to the recalculation of the amorphous phase, they cannot be exactly estimated, a standard deviation of some unit % should be considered.

Samples with intermediate Ni content obtained from zeolite Ni-A (x_{Ni} = 0.31, wt. % Ni in the final NCs = 4.80) and Ni-X (x_{Ni} = 0.45, wt. % Ni in the final NCs = 6.20) (this work)

Samples	Amorphous (%)	Zeolite (%)	Nickel (% wt.) (QPA)	Nickel (% wt) (in Ni^0 NPs; from magnetic data)
NiA735C-12min	47.1	51.0	1.9	2.06(3)
NiA750C-0min	46.7	51.6	1.7	1.40(3)
NiX735C-12 min	53.7	40.8	5.5	4.92(9)
NiX750C-0 min	47.8	46.7	5.5	4.21(5)

Samples with low Ni content obtained from zeolite Ni-A (x_{Ni} = 0.05, wt. % Ni in the final NCs = 1.03) and Ni-X (x_{Ni} = 0.09, wt. % Ni in the final NCs = 1.68) (ref. [18,26])

Samples	Amorphous (%)	Zeolite (%)	Nickel (% wt.) (QPA)	
NiA735C-12min	–	~100[a]	trace	
NiA750C-0min	–	~100[a]	trace	
NiX735C-12 min	–	~100[a]	trace	
NiX750C-0 min	–	~100[a]	trace	

Samples with high Ni content obtained from zeolite Ni-A (x_{Ni} = 0.75, wt. % Ni in the final NCs = 15.0) and Ni-X (x_{Ni} = 0.79, wt. % Ni in the final NCs = 14.4) (ref. [24,25])

Samples	Amorphous (%)	Zeolite (%)	Nickel (% wt.) (QPA)	NiO (% wt.)	HNi_2 (% wt.)
NiA735C-12min	85.9	5.2(2)	7.4(1)	0.8(2)	0.7(2)
NiA750C-0min	83.0	8.5(2)	6.4(5)	1.4(2)	0.7(2)
NiX735C-12 min	84.7	0.3(1)	9.7(1)	5.3(4)	
NiX750C-0 min	84.4	0.3(1)	9.6(1)	5.7(3)	

[a] ~100 means that the XRD pattern of the sample of the Ni-zeolite after the thermal treatment under the reducing atmosphere does not significantly differ from the XRD pattern of the same sample thermally untreated.

A appears more stable as the amorphous phase in the heat-treated samples is slightly lower than that in the samples obtained from zeolite X, (Table 1). There is almost no difference between the two treatment temperatures investigated. Ni^0 particles are present in both series, with values of about 1–2 wt% in A samples and about 4–5 wt% in X samples. Noteworthy, neither the amount of amorphous phase, nor the amount of Ni^0 seems influenced by temperature. The negligible change in both the width of the diffraction peaks and their shape, still sharp in the patterns of the heat-treated samples (see Fig. 2), is an indication of how the crystallinity of the zeolite is maintained after the heat treatments.

As it appears evident from the reported data, the Ni^0 amount present in the NCs after the thermal treatment under a reducing atmosphere is lower than the amount of Ni^{2+} cations originally present in the zeolite. This fact must be ascribed to the incomplete reduction of Ni^{2+} cation rather than to successive re-oxidation, as metallic nanoparticles were proved to be protected against re-oxidation by the ceramic matrix where they are embedded [17,26].

Comparing the results obtained here with the previous works, Scheme 1, the Ni content in the initial zeolite demonstrates to play an important role. Indeed, thermal treatment under a reducing atmosphere does not sensibly damage the microporous zeolite structure at a low Ni content, while for medium Ni content we can observe an amorphization of the sample of about 50% and an almost total destruction of the zeolitic phase at high Ni content.

3.2. Textural and morphological characterization of NiA and NiX zeolites

The textural properties of the NiX nanocomposites, NiX735C-12min and NiX750C-0min, were estimated by N_2 sorption at −196 °C. The N_2 adsorption/desorption isotherms are of type I (Fig. 3a), distinctive of microporous materials, although the presence of a limited desorption hysteresis suggests the presence of small mesopores. In the case of Ni-exchanged zeolite A, the low-temperature N_2 adsorption method gave inaccurate results caused by the very small micropores of zeolite A: the shape of the N_2 isotherm is type II (Figure SI-1), which is generally associated with non-porous or relatively large pores materials [35]. The adsorption of CO_2 at 0 °C was then performed on the nanocomposites derived from NiA zeolite, NiA735C-12min and NiA750C-0min, to overcome the limitation of diffusion linked to the kinetics of the N_2 probe molecule [17,36]. In contrast with N_2 isotherm, the shape of CO_2 isotherm, Fig. 3b, resembles type I, suggesting the presence of very small microporosity.

The textural properties of NiA and NiX nanocomposites, i.e. the values of specific surface area (S_{BET}, $S_{Langmuir}$), total pore volume (V_p) and micropore volume (V_{mp}) are reported in Table 2.

The calcination temperature has a negligible effect on the surface area and porous texture of the nanocomposites, and this is true with both NiA and NiX series. Conversely, the effect of nickel content is fairly visible when comparing values in Table 2 with those in Tables SI–1 obtained for NiA750C-0min e NiX750C-0min with a lower Ni content.

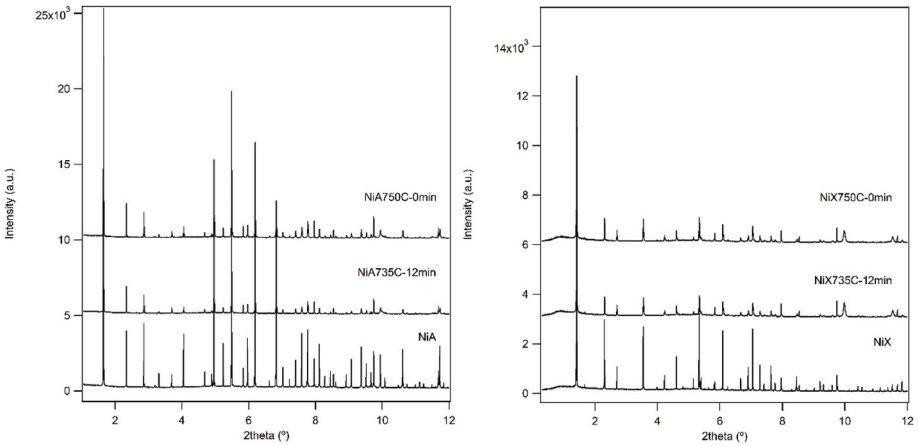

Fig. 2. Diffraction patterns of thermally treated zeolites and their original counterparts.

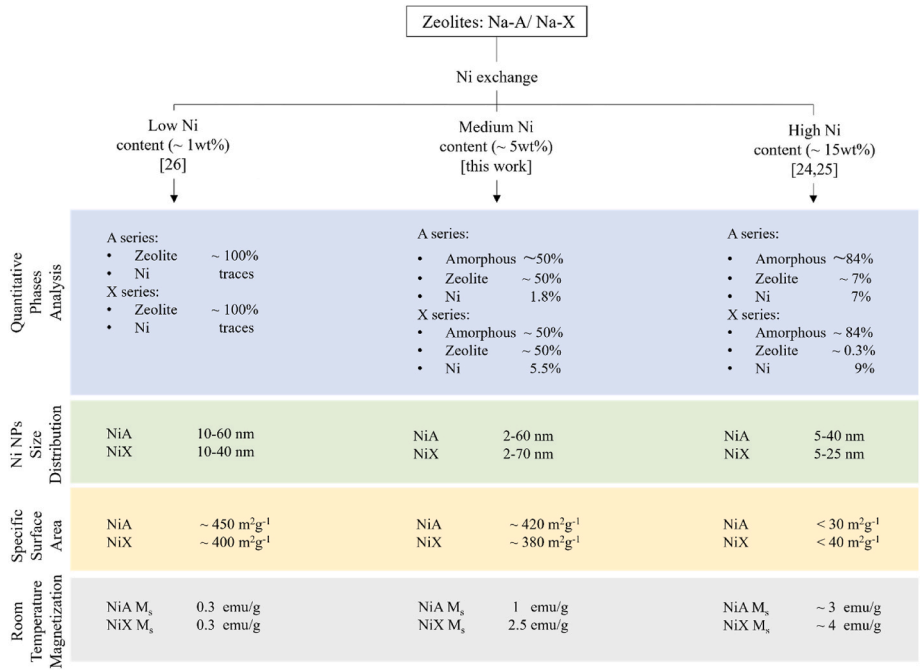

Scheme 1. Effect of Ni content on nanocomposite properties: schematic representation.

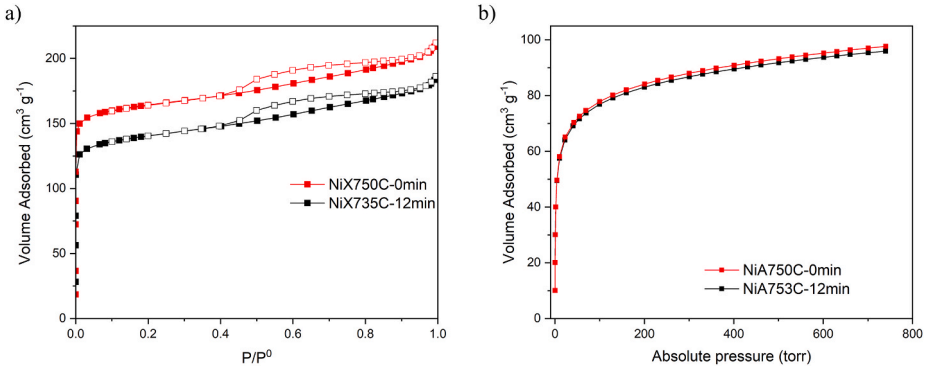

Fig. 3. (a) N_2 adsorption-desorption isotherms at −196 °C of NiX735C-12min and NiX750C-0min and (b) CO_2 adsorption isotherm at 0 °C of NiA735C-12min and NiA750C-0min. Full and empty symbols correspond to adsorption and desorption runs, respectively.

Table 2
Specific surface area, total pore volume (V_p), and micropore volume (V_{mp}) as obtained by N_2 isotherms at −196 °C and CO_2 isotherm at (0 °C).

	N_2 (−196 °C)				CO_2(0 °C)	
	Specific surface area (m^2g^{-1})		V_{mp} (cm^3g^{-1})	V_p (cm^3g^{-1})	Specific surface area (m^2g^{-1})	V_p (cm^3g^{-1})
Sample	S_{BET}[a]	$S_{Langmuir}$	t-plot[b]	Total	DR[c]	DR[c]
NiX735C-12min	397	610	0.16	0.31	–	–
NiX750C-0min	366	686	0.19	0.29	–	–
NiA735C-12min	–	–	–	–	424	0.16
NiA750C-0min	–	–	–	–	418	0.17

[a] Brunauer-Emmet-Teller.
[b] t-plot method.
[c] Dubinin-Radushkevich.

The values of the surface area of the composites at medium Ni content (4.80–6.20 wt%) are systematically lower than those of the composites at lower nickel content (approx. 1 wt%). Furthermore, the hysteresis loop of nitrogen isotherms is more pronounced in the medium-content samples, Fig. 3a, than in the low-content samples, Figure SI-2, indicating an increase in the fraction of mesopores, in agreement with the lower % of the zeolitic structure. The textural properties change while increasing nickel content. Indeed, at high content (approx. 15 wt%), the complete collapse of the zeolitic structure is observed, leading to very low surface area values and a disordered distribution of small and large mesopores, Scheme 1.

HRTEM measurements were carried out on the NiA and NiX nanocomposites to investigate the morphological and structural properties upon different thermal treatments at 735 °C for 12 min and at 750 °C for 0 min under reducing atmosphere. A similar characterization of the as-prepared NiA and NiX zeolites, i.e. before thermal treatments, was reported in a very recent paper [17]. In particular, it was observed that Ni can preserve the crystallinity of either zeolite A or zeolite X. Moreover, highly dispersed small Ni-containing nanoparticles, presumably Ni oxides/hydroxides, with mean diameter $d_m = 1.8 \pm 0.3$ nm for NiA and $d_m = 1.3 \pm 0.2$ nm in the case of NiX, were observed in both samples.

The results of the measurements performed on NiA735C-12min and NiA750C-0min are shown in Fig. 4, Figure SI-3 and Figure SI-4 of the Supporting Information. Upon thermal treatments under reducing atmosphere, small Ni-containing nanoparticles underwent coalescence, giving rise to large globular Ni particles, with some particles with square and irregular shapes. The Ni size ranges between 3.5 and 50 nm for NiA735C-12min, and 3.5 and 60 nm for NiA750C-0min (a, b, d, e and inset in Fig. 4), which results in average diameters $d_m = 9.7 \pm 5.5$ nm and $d_m = 11.0 \pm 5.7$ nm, respectively. Overall the particle size distributions are quite similar (Fig. 4, c vs. f), however, the relative number of particles with size <5 nm is higher in the sample heated at 735 °C compared with sample heated at 750 °C, where the particles with size >30 nm are more abundant. These features reveal a simultaneous effect of the heating temperature and of time at a constant temperature. The EDS analysis indicates a uniform relative spatial distribution of Ni within the A zeolite matrix in both samples, due to the contribution of both small and large Ni particles, as measured in several regions of the nanocomposites (examples are shown in Figure SI-3 and Figure SI-4). Residual Na^+ cations are detected by EDS analysis, these species are likely located in sites of the zeolite framework which are not accessible to small, divalent, strongly hydrated Ni^{2+} cations [17,37].

In addition, the samples display some regions in which the presence of diffraction fringes corresponding to (100) planes of sodium aluminium silicate hydrate cubic phase (JCPDS file number 00-038-0241), which indicates that the production of Ni particles at high temperature under reducing atmosphere did not alter significantly crystallinity of zeolite A (Fig. 4b and inset in c), according to the QPA that revealed that the zeolite (both A and X) crystallinity is maintained after thermal treatments and all the samples contain ~50 wt,% of an amorphous phase.

Overall, the NiX735C-12min and NiX750C-0min samples display similar morphology to the NiA samples, as shown in Fig. 5, Figure SI-5 and Figure SI-6 of the Supporting Information. Notwithstanding, the formed Ni nanoparticles are much more heterogeneous in size, which results in particle size distributions broader than those obtained with the NiA nanocomposites (Fig. 5, c and f). As a consequence, the average diameter size becomes larger i.e. $d_m = 14.0 \pm 10.5$ nm for NiX735C-12min and $d_m = 15.4 \pm 11.7$ nm for NiX750C-0min. The larger size is also reflected in EDS maps of Ni (Figure SI-5 and Figure SI-6), which revealed the contribution of large Ni particles within the X zeolite matrix. In particular, fast heating at 750 °C under reducing atmosphere favoured both formation and agglomeration of Ni particles and gave rise to larger Ni particles, still preserving many particles with size <2.5 nm according to the particle size distribution shown in Fig. 5f. Analogously, the presence of residual Na^+ cations, not exchanged in the preparation, was detected [17].

Both NiX nanocomposites display crystalline regions (Fig. 5, b and e) in which the observed diffraction fringes were ascribed to (111) planes of cubic sodium aluminium silicate hydrate ($Na_{88}Al_{88}Si_{104}O_{384}$ $220H_2O$, JCPDS file number 00-002-0062). Moreover, some large Ni^0 NPs in which the diffraction fringes related to (200) planes of cubic phase (JCPDS file number 00-046-1043), were observed in agreement with XRD findings on the NiX750C-0min sample (Fig. 5, inset of f).

Based on these observations, HRTEM characterization identified a difference in the Ni particle population both as a result of the original zeolite (A or X) and the heat treatment under reducing atmosphere (735 °C for 12 min or 750 °C for 0 min). Moreover, to emphasize the effect of metal loading on the Ni^0 dispersion in final materials, these results are compared with those obtained for nanocomposites with higher [25] and lower [26] Ni content. The comparison is summarised in Table 3.

The differences observed in two families of nanocomposites, derived from A and X zeolites, concerning the Ni homogeneity and size distribution, are correlated (i) firstly to the different structures of the parent materials and (ii) to the Ni content (see Scheme 1). Moreover, the temperature increase from 735 °C up to 750 °C favoured the agglomeration of Ni^0 NPs into larger ones in both A or X zeolite-containing nanocomposites. The temperature effect was not observed the samples with a lower Ni content [26].

Interestingly, nanocomposites with intermediate Ni content, in

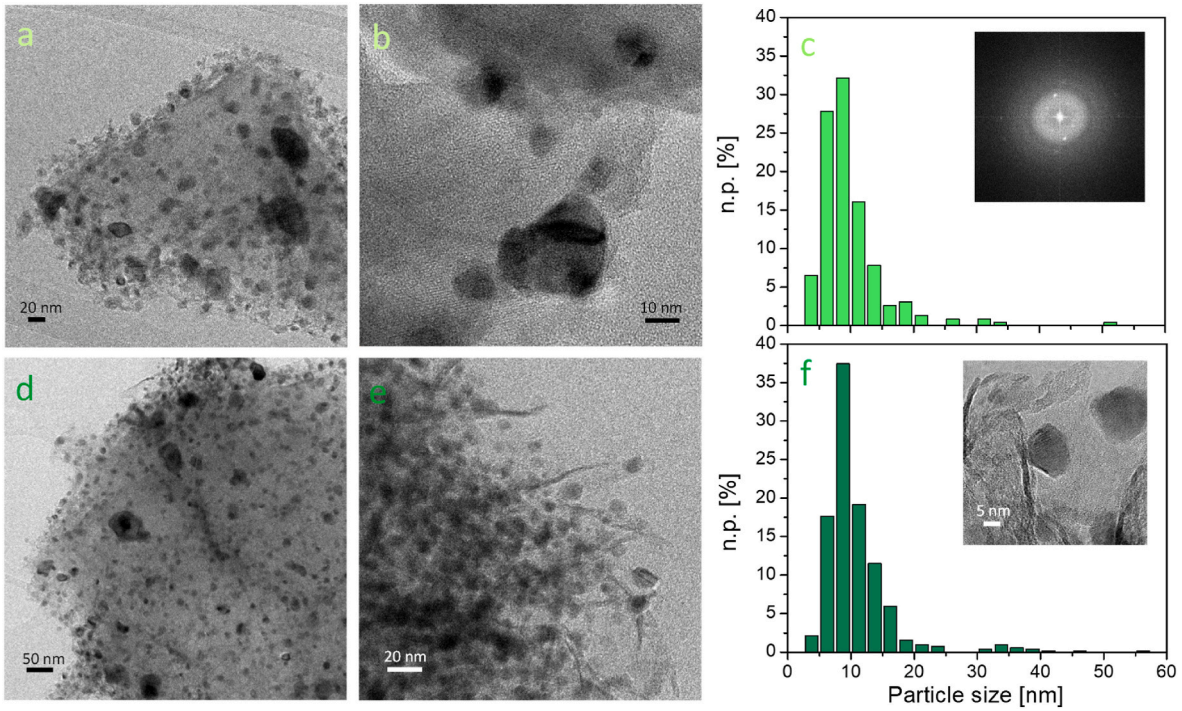

Fig. 4. Representative TEM (a, d, e), HRTEM (b) images and Ni particle size distribution (c, f) of the NiA735C-12min and Ni750C-0min samples, respectively. n.p. [%] = number of counted particles of diameter d_i. Fourier Transform of the image in b (inset in c) of the NiA735C-12min sample. Zoom of big Ni particles (inset in f). Instrumental magnification: 50,000 × (a), 200,000 × (b), 30,000 × (d), 100,000 × (e) and 400,000 × (inset in f).

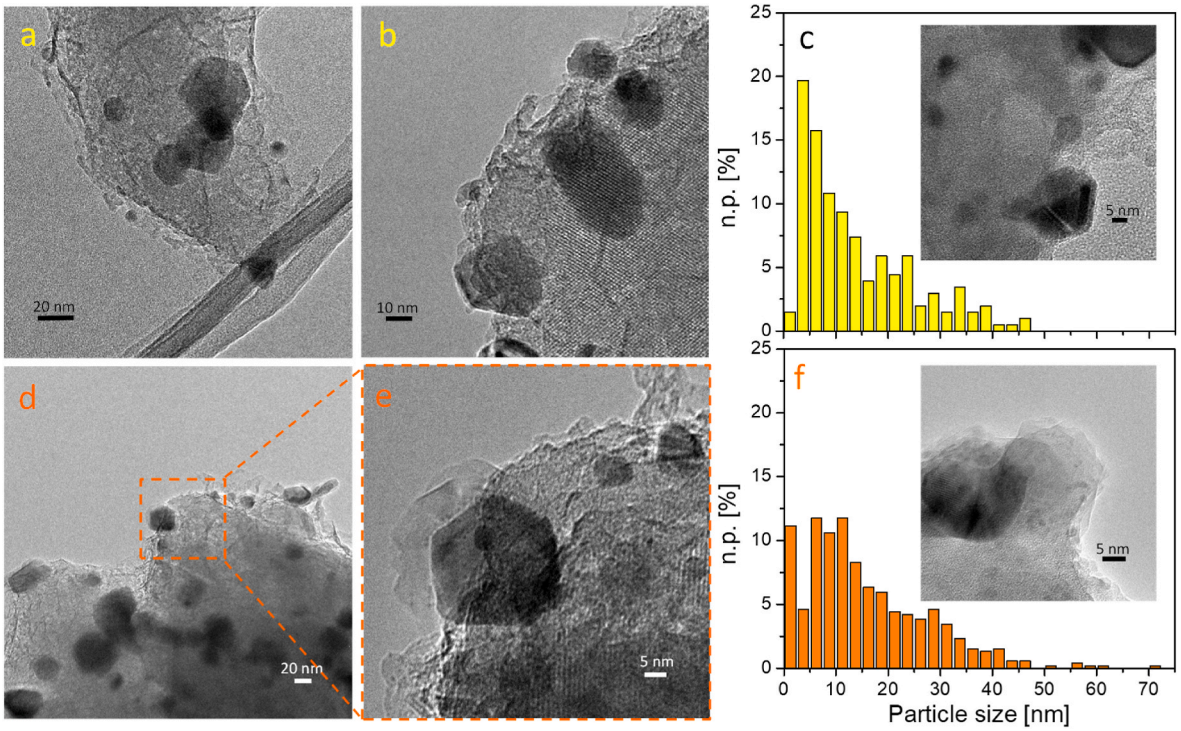

Fig. 5. Representative TEM (a, d), HRTEM (b,e) images and Ni particle size distribution (c, f) of the NiX735C-12min and NiX750C-0min samples, respectively. n.p. [%] = number of counted particles of diameter d_i. Zooms of big Ni particles (insets in c and e). Instrumental magnification: 50,000 × (a,d), 150,000 × (b), 25,000 × (inset in c and e), 100,000 × (e) and 400,000 × (inset in f).

Table 3
Comparison of the Ni size distribution range and average diameter (d_m) obtained for the nanocomposites with low, intermediate and high Ni content.

Ni content	Sample	Ni size distribution range (nm)	Average diameter (nm)	Reference
Low	NiA735C-12min	10–60	16.5 ± 6.5	[26]
	NiA750C-0min	10–35	15.0 ± 5.4	[26]
	NiX735C-12min	10–40	18.0 ± 8.7	[26]
	NiX750C-0min	10 - 40 (some 60, 80)	17.5 ± 9.7	[26]
Intermediate	NiA735C-12min	2.0–50	9.7 ± 5.5	This study
	NiA750C-0min	2.0–60	11.0 ± 5.7	This study
	NiX735C-12min	2.0–50	14 ± 10.5	This study
	NiX750C-0min	2.0–70	15.4 ± 11.7	This study
High	NiA735C-12min	5.0–40	17.6 ± 5.8	[25]
	NiA750C-0min	5.0–30	16.7 ± 4.2	[25]
	NiX735C-12min	5.0–25	12.7 ± 3.7	[25]
	NiX750C-0min	5.0–25	13.5 ± 3.6	[25]

particular X zeolite-derived materials, contain smallest Ni^0 NPs within the series, conversely, the nanocomposites with low Ni content display a great number of NPs with a size around 10 nm mainly located at the zeolite's grain boundaries and/or surfaces [26]. This feature can be explained by considering that the structure of both zeolites was stable after thermal treatments performed to obtain the nanocomposites with low Ni content, according to XRD. It was inferred that the small diameters of the zeolite channels prevent the formation of small Ni^0 NPs to migrate inside the zeolite framework. On the contrary, XRD results indicate that a small percentage of zeolites A and X is still crystalline after thermal treatment in the presence of high Ni content. In these samples, the amorphous matrix did not impede the coalescence of the smallest NPs giving rise to a different population of Ni^0 NPs in nanocomposites [25].

3.3. Magnetic properties

The isothermal magnetization curves of all the studied samples between 2 and 300 K are reported in Fig. SI-7a of the Supplementary Material. Above about 150 K, all *M(H)* curves exhibit a clear saturation effect at high magnetic fields, below 150 K, a linear non-saturating contribution with a slope rapidly increasing with reducing T is observed; at the lowest temperatures such a non-saturating effect displays a strong downward curvature. The ferromagnetic (saturating) magnetization is ascribed to Ni^0 nanoparticles, whereas non-saturating term indicates that a significant fraction of paramagnetic Ni^{2+} ions is still dispersed within zeolite matrix, as already observed in similar systems [23,25]. Starting from the maximum magnetization measured at room temperature (where the paramagnetic spectrum of Ni^{2+} ions is a small signal) assuming that the actual density per Ni atom in Ni^0 particles is the same as in bulk Ni (0.6 Bohr magnetons) [38], it is possible to evaluate how much of the exchanged Ni has been used to form the nanoparticles and how much is still embedded in ionic form in the matrix. The relative amounts of the two quantities are shown in Fig. 6a for all the studied samples. The mechanism of nanoparticle formation turns out to be significantly more efficient in X-zeolites than in A-zeolites; within each subclass, the efficiency of nanoparticle formation is systematically higher in the treatments at the lower temperature for a longer time. The same analysis allows one to obtain the fraction (in wt. %) of exchanged Nickel which is present as Ni^0 in nanoparticles: the results are reported in Table 1 and turn out to be in excellent agreement

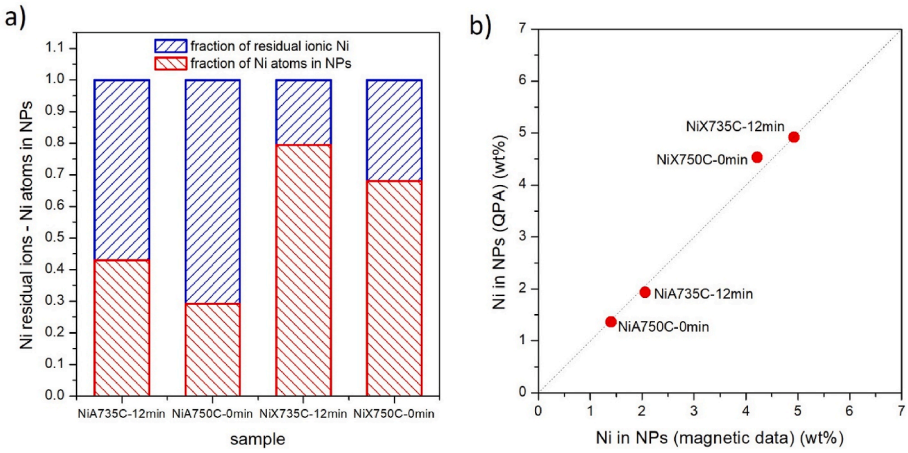

Fig. 6. a) fractions of Ni atoms in Ni^0 nanoparticles and of Ni^{2+} ions embedded in the matrix for all studied samples; b) comparison between estimates of the metallic Ni obtained from magnetic measurements and QPA analysis.

with the ones obtained by QPA analysis (same Table), as shown in Fig. 6b.

The hysteretic properties of the magnetization are put in evidence in Figs. SI–7b of the Supplementary Material, where an expansion of Figs. SI–7a at low fields is shown. Magnetic hysteresis is well represented by the coercive field H_c whose behaviour with temperature is shown in Fig. 7 for all samples in the 2–300 K interval. The slope of the H_c (T) curve is somewhat higher in A-zeolite samples, in agreement with the fact that the nanoparticles are smaller, as shown above by HRTEM analysis. The behaviour of H_c in the Ni-exchanged zeolites containing weakly interacting Ni ions (before any thermal treatment and to the formation of Ni^0 particles) is also reported for comparison. Except for the very low-temperature region (T < 15 K), where a strong coercive field appears [17], H_c is always zero as indeed expected from a paramagnetic system.

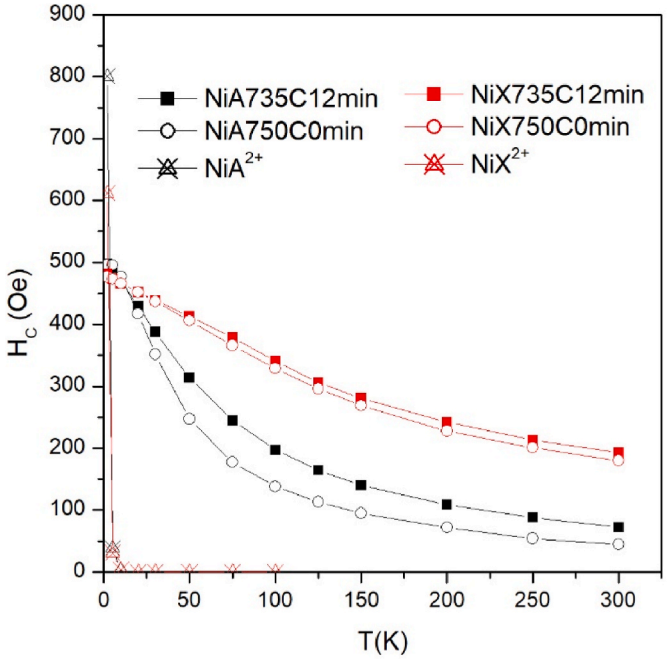

Figure 7

Fig. 7. Behaviour of the coercive field as a function of measurement temperature for all samples. The values of the coercive field measured on the Ni-exchanged zeolites before thermal treatments are reported for comparison.

The FC/ZFC curves measured on all the studied materials under a field of 50 Oe are reported in Figs. SI–8 of the Supplementary Materials. All the observed curves are compatible with the presence of magnetically interacting nanoparticles [39]. Different thermal treatments give rise to curves similar in shape but different in absolute value in the two A-zeolite samples, and similar in both shape and absolute value in the two X-zeolite samples. In the latter samples, the FC/ZFC curves are almost featureless and flat. The present results are in qualitative agreement with the ones obtained with other Ni-exchanged zeolites after thermal treatment [23,25].

The distribution of the blocking energies of either single nanoparticles or small nanoparticles' aggregates (i.e., the individual magnetic units coherently responding to the magnetic field), $p(E_B)$, can be approximately estimated by taking the derivative of the difference between FC and ZFC curves [40]. Such a distribution is shown in Figs. SI–9 of the Supplementary Materials for all the studied samples. The distribution of the sizes of these magnetic units, $p(D_m)$, can be obtained from the same curves by estimating the average value of the effective magnetic anisotropy $<K_{eff}>$ [40]. It should be noted that both intra-particle anisotropies and interparticle interactions concur in determining the value of $<K_{eff}>$ [41]. The quantity $<K_{eff}>$ can be estimated from the coercive field according to the formula $<K_{eff}> \approx <H_c> M_s/2$, where M_s is the saturation magnetization of nanoparticles (obtained from magnetic measurements) and $<H_c>$ is the average value of the coercive field over the entire interval of temperatures (see Fig. 7) [38]. The effective anisotropies turn out to be around $<K_{eff}> = 6.5 \times 10^4$ erg/cm^3 in the A-zeolite samples and close to $<K_{eff}> = 9 \times 10^4$ erg/cm^3 in the X-zeolite samples. The $p(D_m)$ curves obtained using these values are reported in Fig. 8. The upper limit of the region of investigated D_m is dictated by the maximum measurement temperature of FC/ZFC curves, i.e. room temperature.

A comparison of $p(D_m)$ with the histograms for the individual particle sizes obtained by HRTEM (see Figs. 4 and 5) indicates that the magnetic units coherently responding to a magnetic field are not single particles, but small aggregates of magnetically correlated particles; this is in agreement with the observation that the magnetization of all examined materials is non-superparamagnetic, but displays hysteresis even at room temperature (see Figs. SI–7b of the Supplementary Material); nevertheless, the $p(D_m)$ curves keep some features of the individual-particle histograms, being narrower and more structured in A-zeolite samples (with modal value of 17–20 nm) and larger and flatter in X-zeolite samples, without any definite tendency to decrease at high D_m.

The r.t. magnetization M_s of the present samples is of the order of 1

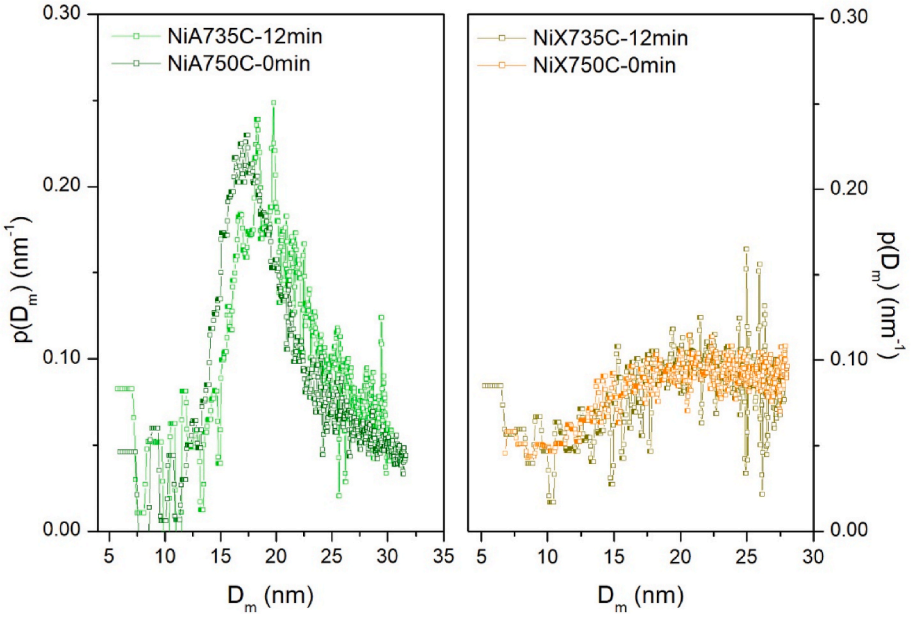

Fig. 8. Size distributions of the magnetic units coherently responding to the field for all samples.

(2.5) emu/g for samples deriving from A (X) zeolites (see Figs. SI–7), whereas $M_s \approx 3$–4 emu/g in samples bearing the highest possible Ni content [25] and $M_s \approx 0.3$ emu/g in weakly loaded zeolites [26], see Scheme 1. It should be remarked that the magnetization value of zeolites loaded with an intermediate Ni concentration turns out to be largely sufficient to guarantee a good response of the materials to a magnetic field gradient, which is a very important aspect in magnetic separation processes.

4. Conclusions

The results concerning the metal-ceramic nanocomposites obtained after thermal treatment under a reducing atmosphere of zeolite Ni-A and Ni-X bearing an intermediate Ni content, and the comparison with the homologous data of the nanocomposites with low [17,26] and high [24, 25] Ni contents, supplied new insights into the extent to which the amount of Ni of the original zeolites affects the thermal transformation and the technological properties of the final products. In particular, it was found that.

1) An excellent agreement between the structural/morphological properties and magnetic results is observed in all the studied cases.
2) The efficiency of conversion of the loaded Ni cations in Ni^0 particles is good, particularly in materials originating from X zeolite, giving rise to a significant magnetization of samples at room temperature.
3) The topology of the starting zeolite has a larger impact than the differences between thermal treatments on the application-oriented magnetic properties of the final materials, such as magnetization and coercive field.
4) Compositional, structural, and textural data of the metal-ceramic nanocomposites with low Ni content do not significantly change as compared to the homologous data of the parent zeolites.
5) The presence of high Ni content in the metal-ceramic nanocomposites gives rise to the almost total collapse of the original, microporous zeolite structure with consequent large variations of the relevant compositional, structural, and textural data as compared to the parent zeolites.
6) An intermediate Ni content in the metal-ceramic nanocomposites results in compositional, structural, and textural data, which can be considered half the way between those of the metal-ceramic nanocomposites with low and high Ni content.

Zeolites are excellent cation exchangers, adsorbents, and catalysts. The validity of zeolites in these fields is largely enhanced if these materials exhibit a sufficiently strong magnetic response. Actually, this property would allow easy recovery of the magnetic cation exchanger, adsorbent, or catalyst from the media where it is used, by simply using an external magnet. The metal-ceramic nanocomposites with low Ni content kept all the properties of the parent zeolites from which they originated. However, they cannot be considered magnetic zeolites as the small amount of Ni^0 nanoparticles present therein does not result in a magnetic response which is adequate to perform the magnetic separation. Conversely, the metal-ceramic nanocomposites with high Ni content exhibit a strong magnetic response suitable for magnetic separation. However, the almost total collapse of the original, microporous zeolite structure results in the overall worsening of cation exchange, adsorption and catalytic properties as compared to the parent zeolites.

The metal-ceramic nanocomposites with intermediate Ni content bear an amount of Ni^0 nanoparticles sufficient for magnetic separation. Moreover, the fact that about 50% of the original zeolite structure is retained makes sure that the cation exchange, adsorption and catalytic properties do not strongly differ from those of the parent zeolites. Thus, the metal-ceramic nanocomposites with intermediate Ni content may be considered “real magnetic zeolites”.

The catalytic properties of the metal-ceramic nanocomposites with intermediate Ni content deserve some more consideration. Acknowledged literature data [42–47] reports that materials obtained by impregnating zeolites Na-A and Na-X with Ni^{2+} salts and by subjecting such Ni^{2+} impregnated zeolites Na-A and Na-X to thermal treatment under a reducing atmosphere, very strongly catalyse the reaction which transforms carbon dioxide into methane. These catalysts were found to bear a Ni content of about 5–15%. These materials are very similar to the metal-ceramic nanocomposites with intermediate Ni content investigated in this work. Moreover, the fact that our metal-ceramic nanocomposites are obtained by Ni^{2+} exchange, rather than by impregnation, as it occurs for catalysts of refs. [43–47] might result in a more advantageous distribution of the Ni^0 nanoparticles within the original, microporous zeolite structure, which could result in an enhanced catalytic action. The catalytic action of the metal-ceramic nanocomposites

with intermediate Ni content toward the reaction, which transforms carbon dioxide into methane will be the topic of a forthcoming work.

Declaration of competing interest

The authors declare that they have no known competing financial interests or personal relationships that could have appeared to influence the work reported in this paper.

Appendix A. Supplementary data

Supplementary data to this article can be found online at https://doi.org/10.1016/j.ceramint.2023.07.003.

References

[1] A.H. Lu, E.L. Salabas, F. Schüth, Magnetic nanoparticles: synthesis, protection, functionalization, and application, Angew. Chem. Int. Ed. 46 (2007) 1222–1244, https://doi.org/10.1002/ANIE.200602866.

[2] M.A. Taha, R.A. Youness, M.F. Zawrah, Review on nanocomposites fabricated by mechanical alloying, Int. J. Miner. Metall. Mater. 26 (2019) 1047–1058, https://doi.org/10.1007/S12613-019-1827-4, 26:9 2019.

[3] P. Mohanty, R. Mahapatra, P. Padhi, C.H.V.V. Ramana, D.K. Mishra, Ultrasonic cavitation: an approach to synthesize uniformly dispersed metal matrix nanocomposites—a review, Nano-Structures & Nano-Objects 23 (2020), 100475, https://doi.org/10.1016/J.NANOSO.2020.100475.

[4] E. Omanović-Mikličanin, A. Badnjević, A. Kazlagić, M. Hajlovac, Nanocomposites: a brief review, Health Technol. 10 (2020) 51–59, https://doi.org/10.1007/S12553-019-00380-X.

[5] B.L. Rivas, B.F. Urbano, J. Sánchez, Water-soluble and insoluble polymers, nanoparticles, nanocomposites and hybrids with ability to remove hazardous inorganic pollutants in water, Front. Chem. 6 (2018) 320, https://doi.org/10.3389/FCHEM.2018.00320/BIBTEX.

[6] B. Ates, S. Koytepe, A. Ulu, C. Gurses, V.K. Thakur, Chemistry, structures, and advanced applications of nanocomposites from biorenewable resources, Chem. Rev. 120 (2020) 9304–9362, https://doi.org/10.1021/ACS.CHEMREV.9B00553/ASSET/IMAGES/MEDIUM/CR9B00553_0052.GIF.

[7] A.V. Rane, K. Kanny, V.K. Abitha, S. Thomas, Methods for synthesis of nanoparticles and fabrication of nanocomposites, Synthesis of Inorganic Nanomaterials (2018) 121–139, https://doi.org/10.1016/B978-0-08-101975-7.00005-1.

[8] T. Guha, G. Gopal, R. Kundu, A. Mukherjee, Nanocomposites for delivering agrochemicals: a comprehensive review, J. Agric. Food Chem. 68 (2020) 3691–3702, https://doi.org/10.1021/ACS.JAFC.9B06982/ASSET/IMAGES/MEDIUM/JF9B06982_0003.GIF.

[9] S. Chen, A. Skordos, V.K. Thakur, Functional nanocomposites for energy storage: chemistry and new horizons, Mater. Today Chem. 17 (2020), 100304, https://doi.org/10.1016/J.MTCHEM.2020.100304.

[10] L.R. Marcelo, J.S. de Gois, A.A. da Silva, D.V. Cesar, Synthesis of iron-based magnetic nanocomposites and applications in adsorption processes for water treatment: a review, Environ. Chem. Lett. (19) (2020) 1229–1274, https://doi.org/10.1007/S10311-020-01134-2, 19:2 2020.

[11] N. Masunga, O.K. Mmelesi, K.K. Kefeni, B.B. Mamba, Recent advances in copper ferrite nanoparticles and nanocomposites synthesis, magnetic properties and application in water treatment: review, J. Environ. Chem. Eng. 7 (2019), 103179, https://doi.org/10.1016/J.JECE.2019.103179.

[12] S.S. Bristy, M.A. Rahman, K. Tauer, H. Minami, H. Ahmad, Preparation and characterization of magnetic γ-Al2O3 ceramic nanocomposite particles with variable Fe3O4 content and modification with epoxide functional polymer, Ceram. Int. 44 (2018) 3951–3959, https://doi.org/10.1016/J.CERAMINT.2017.11.187.

[13] A. Talaat, M.V. Suraj, K. Byerly, A. Wang, Y. Wang, J.K. Lee, P.R. Ohodnicki, Review on soft magnetic metal and inorganic oxide nanocomposites for power applications, J. Alloys Compd. 870 (2021), 159500, https://doi.org/10.1016/J.JALLCOM.2021.159500.

[14] A. Maleki, A.R. Taherizadeh, H.K. Issa, B. Niroumand, A.R. Allafchian, A. Ghaei, Development of a new magnetic aluminum matrix nanocomposite, Ceram. Int. 44 (2018) 15079–15085, https://doi.org/10.1016/J.CERAMINT.2018.05.141.

[15] N.H. Abdullah, K. Shameli, E.C. Abdullah, L.C. Abdullah, Solid matrices for fabrication of magnetic iron oxide nanocomposites: synthesis, properties, and application for the adsorption of heavy metal ions and dyes, Compos. B Eng. 162 (2019) 538–568, https://doi.org/10.1016/J.COMPOSITESB.2018.12.075.

[16] S. Ronchetti, E.A. Turcato, A. Delmastro, S. Esposito, C. Ferone, M. Pansini, B. Onida, D. Mazza, Study of the thermal transformations of Co- and Fe-exchanged zeolites A and X by "in situ" XRD under reducing atmosphere, Mater. Res. Bull. 45 (2010) 744–750, https://doi.org/10.1016/j.materresbull.2010.02.006.

[17] G. Barrera, P. Allia, P. Tiberto, O. Tammaro, M. Pansini, A. Marocco, M. Manzoli, G. Confalonieri, R. Arletti, S. Esposito, Magnetic clustering of weakly interacting Ni-ions in Ni-exchanged zeolites, Microporous Mesoporous Mater. 335 (2022), 111786, https://doi.org/10.1016/J.MICROMESO.2022.111786.

[18] G. Barrera, P. Tiberto, P. Allia, B. Bonelli, S. Esposito, A. Marocco, M. Pansini, Y. Leterrier, Magnetic properties of nanocomposites, Appl. Sci. 9 (2019) 212, https://doi.org/10.3390/app9020212.

[19] M. Pansini, G. Dell'Agli, A. Marocco, P.A. Netti, E. Battista, V. Lettera, P. Vergara, P. Allia, B. Bonelli, P. Tiberto, et al., Preparation and characterization of magnetic and porous metal-ceramic nanocomposites from a zeolite precursor and their application for DNA separation, J. Biomed. Nanotechnol. 13 (2017) 337–348, https://doi.org/10.1166/JBN.2017.2345.

[20] M. Pansini, F. Sannino, A. Marocco, P. Allia, P. Tiberto, G. Barrera, M. Polisi, E. Battista, P.A. Netti, S. Esposito, Novel process to prepare magnetic metal-ceramic nanocomposites from zeolite precursor and their use as adsorbent of agrochemicals from water, J. Environ. Chem. Eng. 6 (2018) 527–538, https://doi.org/10.1016/J.JECE.2017.12.030.

[21] F.S. Freyria, A. Marocco, S. Esposito, B. Bonelli, G. Barrera, P. Tiberto, P. Allia, P. Oudayer, A. Roggero, J.C. Matéo-Vélez, et al., Simulated moon agglutinates obtained from zeolite precursor using a low-cost and scalable synthesis method, ACS Earth Space Chem 3 (2019) 1884–1895, https://doi.org/10.1021/acsearthspacechem.9b00042.

[22] M. Manzoli, O. Tammaro, A. Marocco, B. Bonelli, G. Barrera, P. Tiberto, P. Allia, J. C. Matéo-Vélez, A. Roggero, E. Dantras, et al., New insights in the production of simulated moon agglutinates: the use of natural zeolite-bearing rocks, ACS Earth Space Chem 5 (2021) 1631–1646, https://doi.org/10.1021/ACSEARTHSPACECHEM.1C00118/SUPPL_FILE/SP1C00118_SI_001.PDF.

[23] F. Sannino, M. Pansini, A. Marocco, A. Cinquegrana, S. Esposito, O. Tammaro, G. Barrera, P. Tiberto, P. Allia, D. Pirozzi, Removal of sulfanilamide by tailor-made magnetic metal-ceramic nanocomposite adsorbents, J. Environ. Manag. 310 (2022), 114701, https://doi.org/10.1016/J.JENVMAN.2022.114701.

[24] S. Esposito, G. Dell'Agli, A. Marocco, B. Bonelli, P. Allia, P. Tiberto, G. Barrera, M. Manzoli, R. Arletti, M. Pansini, Magnetic metal-ceramic nanocomposites obtained from cation-exchanged zeolite by heat treatment in reducing atmosphere, Microporous Mesoporous Mater. 268 (2018) 131–143, https://doi.org/10.1016/j.micromeso.2018.04.024.

[25] G. Barrera, P. Tiberto, S. Esposito, A. Marocco, B. Bonelli, M. Pansini, M. Manzoli, P. Allia, Magnetic clustering of Ni2+ ions in metal-ceramic nanocomposites obtained from Ni-exchanged zeolite precursors, Ceram. Int. 44 (2018) 17240–17250, https://doi.org/10.1016/J.CERAMINT.2018.06.182.

[26] G. Barrera, P. Allia, B. Bonelli, S. Esposito, F.S. Freyria, M. Pansini, A. Marocco, G. Confalonieri, R. Arletti, P. Tiberto, Magnetic behavior of Ni nanoparticles and Ni2+ ions in weakly loaded zeolitic structures, J. Alloys Compd. 817 (2020), 152776, https://doi.org/10.1016/J.JALLCOM.2019.152776.

[27] C. Baerlocher, W.M. Meier, D.H. Olson, MAZ. Atlas of Zeolite Framework Types, 2001, pp. 174–175.

[28] F. Sannino, S. Ruocco, A. Marocco, S. Esposito, M. Pansini, Cyclic process of simazine removal from waters by adsorption on zeolite H-Y and its regeneration by thermal treatment, J. Hazard Mater. 229–230 (2012) 354–360, https://doi.org/10.1016/J.JHAZMAT.2012.06.011.

[29] N.J. Clayden, S. Esposito, C. Ferone, M. Pansini, 29SI and 27Al NMR study of the thermal transformation of barium exchanged zeolite-A to celsian, J. Mater. Chem. 13 (2003) 1681–1685, https://doi.org/10.1039/b212717b.

[30] S. Esposito, G. Dell'Agli, A. Marocco, M. B.B, Undefined Magnetic Metal-Ceramic Nanocomposites Obtained from Cation-Exchanged Zeolite by Heat Treatment in Reducing Atmosphere, Elsevier, 2018.

[31] C. Ferone, B. Liguori, A. Marocco, S. Anaclerio, M. Pansini, C. Colella, Monoclinic (Ba, Sr)-Celsian by thermal treatment of (Ba, Sr)-Exchanged zeolite A, Microporous Mesoporous Mater. 134 (2010) 65–71, https://doi.org/10.1016/J.MICROMESO.2010.05.008.

[32] A. Basile, G. Cacciola, C. Colella, L. Mercadante, M. Pansini, Thermal conductivity of natural zeolite-PTFE composites, Heat Recovery Syst. CHP 12 (1992) 497–503, https://doi.org/10.1016/0890-4332(92)90018-D.

[33] A.F. Gualtieri, E. Mazzucato, P. Venturelli, A. Viani, P. Zannini, L. Petras, X-ray powder diffraction quantitative analysis performed in situ at high temperature: application to the determination of NiO in ceramic pigments, J. Appl. Crystallogr. 32 (1999) 808–813, https://doi.org/10.1107/S0021889899005853.

[34] A.A. Coelho, TOPAS and TOPAS-academic: an optimization program integrating computer algebra and crystallographic objects written in C++, J. Appl. Crystallogr. 51 (2018) 210–218, https://doi.org/10.1107/S1600576718000183.

[35] M. Thommes, K. Kaneko, A.V. Neimark, J.P. Olivier, F. Rodriguez-Reinoso, J. Rouquerol, K.S.W. Sing, Physisorption of gases, with special reference to the evaluation of surface area and pore size distribution (IUPAC technical report), Pure Appl. Chem. 87 (2015) 1051–1069, https://doi.org/10.1515/pac-2014-1117.

[36] K.J. Hwang, W.S. Choi, S.H. Jung, Y.J. Kwon, S. Hong, C. Choi, J.W. Lee, W. G. Shim, Synthesis of zeolitic material from basalt rock and its adsorption properties for carbon dioxide, RSC Adv. 8 (2018) 9524–9529, https://doi.org/10.1039/C8RA00788H.

[37] S. Esposito, A. Marocco, G. Dell'Agli, B. De Gennaro, M. Pansini, Relationships between the water content of zeolites and their cation population, Microporous Mesoporous Mater. 202 (2015) 36–43, https://doi.org/10.1016/J.MICROMESO.2014.09.041.

[38] Cullity, B.D.; Graham, C.D. INTRODUCTION TO MAGNETIC MATERIALS Second Edition.

[39] P. Allia, G. Barrera, P. Tiberto, Linearized rate-equation approach for double-well systems: cooling- and temperature-dependent low-field magnetization of magnetic nanoparticles, Phys. Rev. B 98 (2018), 134423, https://doi.org/10.1103/PhysRevB.98.134423.

[40] H. Mamiya, M. Ohnuma, I. Nakatani, T. Furubayashim, Extraction of blocking temperature distribution from zero-field-cooled and field-cooled magnetization

curves, IEEE Trans. Magn. 41 (2005) 3394–3396, https://doi.org/10.1109/TMAG.2005.855205.
[41] G. Barrera, P. Allia, P. Tiberto, Dipolar interactions among magnetite nanoparticles for magnetic hyperthermia: a rate-equation approach, Nanoscale 13 (2021) 4103–4121, https://doi.org/10.1039/D0NR07397K.
[42] G. Herzer, Anisotropies in soft magnetic nanocrystalline alloys, J. Magn. Magn Mater. 294 (2005) 99–106, https://doi.org/10.1016/J.JMMM.2005.03.020.
[43] N.A. Sholeha, S. Mohamad, H. Bahruji, D. Prasetyoko, N. Widiastuti, N.A. Abdul Fatah, A.A. Jalil, Y.H. Taufiq-Yap, Enhanced CO2 methanation at mild temperature on Ni/zeolite from kaolin: effect of metal–support interface, RSC Adv. 11 (2021) 16376–16387, https://doi.org/10.1039/D1RA01014J.
[44] L. Wei, W. Haije, N. Kumar, J. Peltonen, M. Peurla, H. Grenman, W. de Jong, Influence of nickel precursors on the properties and performance of Ni impregnated zeolite 5A and 13X catalysts in CO2 methanation, Catal. Today 362 (2021) 35–46, https://doi.org/10.1016/J.CATTOD.2020.05.025.
[45] M.C. Bacariza, R. Bértolo, I. Graça, J.M. Lopes, C. Henriques, The effect of the compensating cation on the catalytic performances of Ni/USY zeolites towards CO2 methanation, J. CO2 Util. 21 (2017) 280–291, https://doi.org/10.1016/J.JCOU.2017.07.020.
[46] S. Upasen, G. Sarunchot, N. Srira-ngam, Y. Poo-arporn, P. Wattanachai, P. Praserthdam, P. Ngaotrakanwiwat, J. Panpranot, S. Soisuwan, What if zeolite LTA4A and zeolite LTA5A used as nickel catalyst supports for recycling carbon dioxide to green fuel methane, J. CO2 Util. 55 (2022), 101803, https://doi.org/10.1016/J.JCOU.2021.101803.
[47] J.F. da Costa-Serra, C. Cerdá-Moreno, A. Chica, Zeolite-supported Ni catalysts for CO2 methanation: effect of zeolite structure and Si/Al ratio, Appl. Sci. 10 (2020) 5131, https://doi.org/10.3390/APP10155131. Page 5131 2020, 10.